

# Efficient and Stable All-Inorganic CsPbIBr<sub>2</sub> Perovskite Solar Cells Enabled by Dynamic Vacuum-Assisted Low-Temperature Engineering

Junyi Huang, Shenghua He, Wenzhi Zhang, Aziz Saparbaev, Yi Wang, Yueyue Gao,\* Luwen Shang, Guohua Dong,\* Lobar Nurumbetova, Gentian Yue,\* and Yongguang Tu

Among all-inorganic perovskite photoactive materials, CsPbIBr<sub>2</sub> demonstrates the most balanced trade-off between optical bandgap and phase stability. However, the poor quality and high-temperature engineering of CsPbIBr<sub>2</sub> film hinder the further optimization of derived perovskite solar cells (PSCs). Herein, a simple dynamic vacuum-assisted low-temperature engineering (merely 140 °C) is proposed to prepare high-quality CsPbIBr<sub>2</sub> film (VALT-CsPbIBr<sub>2</sub> film). Compared to HT-CsPbIBr<sub>2</sub> film processed via conventionally high temperature (280 °C), VALT-CsPbIBr<sub>2</sub> film presents higher crystallinity and more full coverage consisting of larger grains and fewer grain boundaries, which results in intensified light-harvesting capability, reduced defects, and extended charge carrier lifetime. Benefiting from those improved merits, VALT-CsPbIBr<sub>2</sub> PSCs show lower trap-state densities, more proficient charge dynamics, and larger built-in potential than HT-CsPbIBr<sub>2</sub> PSCs. Consequently, VALT-CsPbIBr<sub>2</sub> PSCs deliver a higher efficiency of 11.01% accompanied by a large open-circuit voltage of 1.289 V and a remarkable fill factor of 75.31%, being highly impressive among those reported CsPbIBr<sub>2</sub> PSCs. By contrast, the efficiency of HT-CsPbIBr<sub>2</sub> PSCs is only 9.00%. Moreover, VALT-CsPbIBr<sub>2</sub> PSCs present stronger endurance against heat and moisture than HT-CsPbIBr<sub>2</sub> PSCs. Herein, a feasible avenue to fabricate efficient yet stable all-inorganic PSCs via low-temperature engineering is provided.

technology.<sup>[1,2]</sup> More importantly, the state-of-the-art power conversion efficiency (PCE) of hybrid PSCs has surpassed 25%, which is even comparable with commercial silicon solar cells.<sup>[3,4]</sup> However, those photoactive materials of hybrid PSCs are intrinsically unstable under thermal, photo, and moisture stresses due to their fragile organic components featuring volatile and hygroscopic characteristics, i.e., CH<sub>3</sub>NH<sub>3</sub><sup>+</sup>, CH<sub>3</sub>(NH<sub>2</sub>)<sub>2</sub><sup>+</sup>.<sup>[5–8]</sup> The unfavorable features of organic components inevitably deteriorate the long-term operational stability of hybrid PSCs.<sup>[9]</sup> Therefore, seeking other types of photoactive materials featuring superior stability yet high performance is of great urgency for realizing the practical application of PSCs.

Recently, completely substituting organic components in organic–inorganic hybrid photoactive materials with inorganic constituents is gradually paid ever-increasing attention for their excellent stability and great potential for fabricating efficient PSCs especially tandem solar cells.<sup>[10,11]</sup> Up to now, several dominant

types of all-inorganic photoactive materials, such as CsPbBr<sub>3</sub>, CsPbI<sub>3</sub>, CsPbI<sub>2</sub>Br, and CsPbIBr<sub>2</sub>, have been extensively investigated. Among them, CsPbBr<sub>3</sub> presents superior phase stability even without encapsulation, while the large bandgap (≈2.30 eV) weakens their light-harvesting capability and then limits the efficiency of derived PSCs.<sup>[12]</sup> Moreover, CsPbI<sub>3</sub> and

## 1. Introduction


Organic–inorganic hybrid perovskite solar cells (PSCs) have drawn unprecedented interest in academia and industries due to their intrinsic advantages, i.e., excellent absorption coefficient, low exciton binding energy, and facile solution fabrication

J. Huang, S. He, Y. Gao, L. Shang, G. Yue  
Key Laboratory of Photovoltaic Materials  
Henan University  
Kaifeng 475004, P. R. China  
E-mail: gaoyueyue@henu.edu.cn; yuegentian@henu.edu.cn

W. Zhang, G. Dong  
College of Chemistry and Chemical Engineering & Technology Innovation  
Center of Industrial Hemp for State Market Regulation  
Qiqihar University  
Qiqihar 161006, P. R. China  
E-mail: ghdong@qqhru.edu.cn

A. Saparbaev, L. Nurumbetova  
Institute of Ion-Plasma and Laser Technologies  
Uzbekistan Academy of Sciences  
33, Durmon Yuli St., Tashkent 100125, Uzbekistan

Y. Wang, Y. Tu  
Shanxi Institute of Flexible Electronics  
Northwestern Polytechnical University  
Xi'an 710072, P. R. China

 The ORCID identification number(s) for the author(s) of this article can be found under <https://doi.org/10.1002/solr.202100839>.

DOI: 10.1002/solr.202100839

CsPbI<sub>2</sub>Br possess a relatively narrow bandgap of ~1.73 eV and ≈1.92 eV, respectively, leading to highly enhanced light-harvesting ability and impressive efficiency for corresponding PSCs.<sup>[13,14]</sup> Unfortunately, both CsPbI<sub>3</sub> and CsPbI<sub>2</sub>Br easily transform to the yellow non-photoactive orthorhombic phase ( $\delta$ -phase) from the black photoactive phase ( $\alpha$ -phase) under room temperature with a humid environment.<sup>[15]</sup> In contrast, CsPbI<sub>2</sub>Br<sub>2</sub> featuring an appropriate bandgap of ≈2.05 eV and good phase stability even at high temperatures over 400 °C should be a better choice for the practical application of derived PSCs.<sup>[16]</sup> Nevertheless, the efficiency of CsPbI<sub>2</sub>Br<sub>2</sub> PSCs is far from its theoretical value, and even lags behind other all-inorganic counterparts.<sup>[17,18]</sup> Hence, developing feasible methods for further improving the efficiency of CsPbI<sub>2</sub>Br<sub>2</sub> devices is eager to strengthen its competitiveness in the field of PSCs.

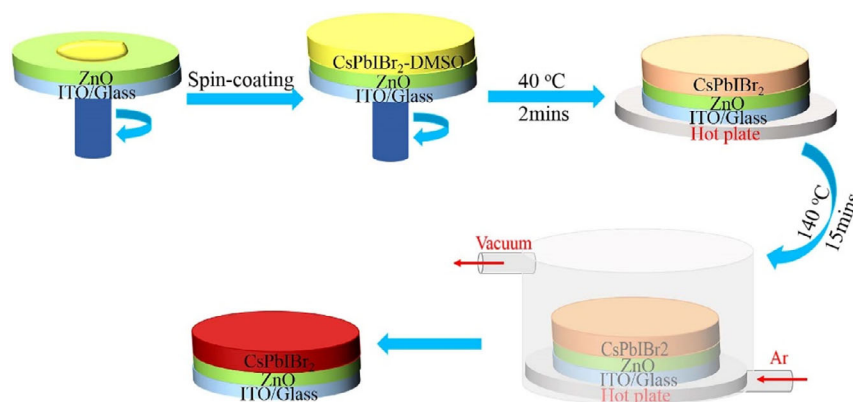
To date, great efforts have been paid to optimize the CsPbI<sub>2</sub>Br<sub>2</sub> film and the corresponding PSCs. Zhu et al. proposed an intermolecular exchange strategy to optimize the CsPbI<sub>2</sub>Br<sub>2</sub> film to suppress charge recombination and prompt charge carrier extraction, which results in a modest PCE of 9.16%.<sup>[19]</sup> Then, Wang and coworkers incorporated sulfamic acid sodium salt into the CsPbI<sub>2</sub>Br<sub>2</sub> film to produce an additional internal electric field to improve the electron transport and injection, thus imparting a good PCE of 10.57%.<sup>[20]</sup> Beyond that, Du and colleagues adopted (NiCo)<sub>1-y</sub>Fe<sub>y</sub>O<sub>x</sub> nanoparticle as a p-doping agent to modify graphene oxide as hole transporting material, which could efficiently boost hole extraction between CsPbI<sub>2</sub>Br<sub>2</sub> film and electrode, producing a high PCE of 10.95%.<sup>[21]</sup> Although progressive achievements have been obtained for CsPbI<sub>2</sub>Br<sub>2</sub> PSCs, the corresponding recorded value of CsPbI<sub>2</sub>Br<sub>2</sub> PSCs is still far from satisfactory. In addition, those high-performance CsPbI<sub>2</sub>Br<sub>2</sub> PSCs are always dependent on a high temperature process for either electron transport layer (ETL, ≥450 °C) or CsPbI<sub>2</sub>Br<sub>2</sub> film (≥200 °C), which not only increases the energy payback time and the production cost but also highly limits the application of CsPbI<sub>2</sub>Br<sub>2</sub> on flexible optoelectronic devices.<sup>[22–28]</sup> Therefore, exploiting a facile low-temperature fabrication process yet further improving the photovoltaic performance of CsPbI<sub>2</sub>Br<sub>2</sub> PSCs should be highly imperative for its development.

Herein, we adopted a simple dynamic vacuum-assisted low-temperature (merely 140 °C) processing technology to prepare high-quality CsPbI<sub>2</sub>Br<sub>2</sub> film (VALT-CsPbI<sub>2</sub>Br<sub>2</sub> film). Compared

to HT-CsPbI<sub>2</sub>Br<sub>2</sub> film processed via conventionally high temperature (280 °C), VALT-CsPbI<sub>2</sub>Br<sub>2</sub> film presents higher crystallinity, fewer grain boundaries, and more uniform coverage upon the substrate, which results in stronger light-harvesting capability, fewer defects, and longer charge carrier lifetime. The abovementioned improved merits impart lower trap-state densities, more proficient charge dynamics, and larger built-in potential for VALT-CsPbI<sub>2</sub>Br<sub>2</sub> PSCs versus that of HT-CsPbI<sub>2</sub>Br<sub>2</sub> ones. As a result, VALT-CsPbI<sub>2</sub>Br<sub>2</sub> PSCs deliver a higher PCE of 11.01% accompanied by a large open-circuit voltage ( $V_{oc}$ ) of 1.289 V and a remarkable fill factor (FF) of 75.31% relative to that of HT-CsPbI<sub>2</sub>Br<sub>2</sub> ones (PCE = 9.00%). Moreover, the unencapsulated VALT-CsPbI<sub>2</sub>Br<sub>2</sub> PSCs could retain over 87% of their initial PCE after being continuously heated at 80 °C in an inert atmosphere for 8 days versus that of HT-CsPbI<sub>2</sub>Br<sub>2</sub> PSCs (62%). Meanwhile, the unencapsulated VALT-CsPbI<sub>2</sub>Br<sub>2</sub> PSCs could remain 65% of their initial PCE under high humidity (≈50%) for 160 h, while HT-CsPbI<sub>2</sub>Br<sub>2</sub> devices are completely out of operation under the same condition. Therefore, compared to HT-CsPbI<sub>2</sub>Br<sub>2</sub> devices, the superior photovoltaic performance coupled with robust stability against heat and humidity of VALT-CsPbI<sub>2</sub>Br<sub>2</sub> PSCs demonstrate the effectiveness of the dynamic vacuum-assisted low-temperature engineering proposed in this work.

## 2. Result and Discussion

The dynamic vacuum-assisted low-temperature process engineering of preparing CsPbI<sub>2</sub>Br<sub>2</sub> film is illustrated in **Scheme 1**. As shown, the CsPbI<sub>2</sub>Br<sub>2</sub> precursor solution in dimethyl sulfoxide (DMSO) was first spin-coated upon ZnO film prepared according to the reported work.<sup>[29]</sup> Then, the as-prepared film was first annealed on a hot plate at 40 °C for 2 min for uniform nucleation-grown process and subsequently settled into a vacuum chamber to remove the residual DMSO molecule for boosting rapid crystallization of CsPbI<sub>2</sub>Br<sub>2</sub> film.<sup>[13]</sup> With the aim of obtaining the optimized morphology of CsPbI<sub>2</sub>Br<sub>2</sub> film, the vacuum-assisted annealing process was carefully controlled via simultaneously vacuuming and inflowing pure argon (Ar) to maintain the pressure at 50–100 Pa and keep the annealing temperature at 140 °C (Figure S1–S3, Supporting Information).<sup>[30–32]</sup> After that, the smooth VALT-CsPbI<sub>2</sub>Br<sub>2</sub> film was obtained and



**Scheme 1.** The schematic illustration of the dynamic vacuum-assisted low-temperature engineering for preparing VALT-CsPbI<sub>2</sub>Br<sub>2</sub> film.

presented a shiny dark-red color versus that of HT-CsPbIBr<sub>2</sub> film prepared via conventionally high temperature (280 °C).

To first provide insight into the morphological difference between HT-CsPbIBr<sub>2</sub> film and VALT-CsPbIBr<sub>2</sub> film, the scanning electron microscopy (SEM), atomic force microscopy (AFM), and Kelvin probe force microscopy (KPFM) were synergistically implemented. As displayed in **Figure 1a**, the HT-CsPbIBr<sub>2</sub> film presents discontinuous distribution with obvious pinholes as well as heterogeneous grains, resulting in a nonuniform and coarse surface featuring a large root mean square (RMS) roughness of 27.4 nm (Figure 1b), which is similar to the CsPbIBr<sub>2</sub> film reported by previous work.<sup>[33–35]</sup> Note that the poor morphology of HT-CsPbIBr<sub>2</sub> film would not only result in numerous shunting paths to induce unfavorable interfacial charge recombination but also endow moisture and oxygen molecules more facile possibilities to invade into HT-CsPbIBr<sub>2</sub> film. Naturally, the abovementioned disadvantages of HT-CsPbIBr<sub>2</sub> film would deteriorate the efficiency and stability of derived devices.<sup>[36]</sup>

In contrast, the VALT-CsPbIBr<sub>2</sub> film showed a full-coverage surface accompanied by highly uniform and crystalline grains possessing sizes in the range of hundreds of nanometers (Figure 1d). Meanwhile, VALT-CsPbIBr<sub>2</sub> crystals are closely compacted via triple-junction grain boundaries to form an almost equal vertex angle with a value of 120°, demonstrating their crystals featuring an equilibrium state with low internal stress, which could be conducive to enhancing the stability of VALT-CsPbIBr<sub>2</sub>.<sup>[19]</sup> Moreover, the VALT-CsPbIBr<sub>2</sub> film depicts a homogeneous and smooth surface with small RMS roughness of 16.5 nm (Figure 1e), which benefits obtaining small interfacial resistance and is conducive to facilitating charge transfer.<sup>[37,38]</sup>

Beyond that, both HT-CsPbIBr<sub>2</sub> film and VALT-CsPbIBr<sub>2</sub> film present uniform contact surface potential (CSP) distribution (Figure 1c,f). However, the average CSP of VALT-CsPbIBr<sub>2</sub> film is nearly reduced by ≈0.30 V versus that of HT-CsPbIBr<sub>2</sub> film, which indicates the larger work function of VALT-CsPbIBr<sub>2</sub>

film.<sup>[39]</sup> Generally, the enhanced work function of VALT-CsPbIBr<sub>2</sub> film is ascribed to its fewer compositional defects caused by its weaker n-type doping, which is corroborated by the preferable stoichiometric ratios of VALT-CsPbIBr<sub>2</sub> film versus that of HT-CsPbIBr<sub>2</sub> obtained from the X-ray photoelectron spectroscopy (XPS) result (Figure S4, Supporting Information). The larger work function of VALT-CsPbIBr<sub>2</sub> film is not only beneficial for improving the structural stability of VALT-CsPbIBr<sub>2</sub> but also profitable to obtain a larger built-in potential for derived devices.<sup>[40,41]</sup>

As exhibited in **Figure 2a**, HT-CsPbIBr<sub>2</sub> displays two distinct X-ray diffraction (XRD) peaks at 14.88° and 29.95°, respectively, which are indexed to (100) and (200) crystal planes of α-phase CsPbIBr<sub>2</sub>.<sup>[42]</sup> It is noticed that other diffraction peaks correlating with (110) and (210) crystal planes of α-phase CsPbIBr<sub>2</sub> are absent, implying that HT-CsPbIBr<sub>2</sub> possesses a preferentially crystalline orientation along the (100) crystal plane, which is perpendicular to the substrate and favorable for charge transport.<sup>[43,44]</sup> Except for featuring characteristics as same as HT-CsPbIBr<sub>2</sub>, VALT-CsPbIBr<sub>2</sub> presents stronger diffraction intensities along with smaller full width at half maximum and slightly shift to a small angle (Table S1, Supporting Information), revealing VALT-CsPbIBr<sub>2</sub> having higher crystallinity and larger crystal size, which is consistent well with its SEM image.

The ultraviolet photoelectron spectroscopy measurement was conducted to investigate the electronic energy level of HT-CsPbIBr<sub>2</sub> and VALT-CsPbIBr<sub>2</sub>. As shown in Figure 2b and Figure S5, Supporting Information, the valence band maximum (VBM) could be deduced to −5.27 and −5.36 eV for HT-CsPbIBr<sub>2</sub> and VALT-CsPbIBr<sub>2</sub> according to VBM = 21.22 − (E<sub>cutoff</sub> − E<sub>onset</sub>), respectively.<sup>[23]</sup> Then the conduction band minimum (CBM) could be calculated based on CBM = VBM + E<sub>opt</sub> (optical bandgap) (Figure S6, Supporting Information), corresponding to −3.19 and −3.31 eV for HT-CsPbIBr<sub>2</sub> and VALT-CsPbIBr<sub>2</sub>, respectively. Compared to HT-CsPbIBr<sub>2</sub>, the

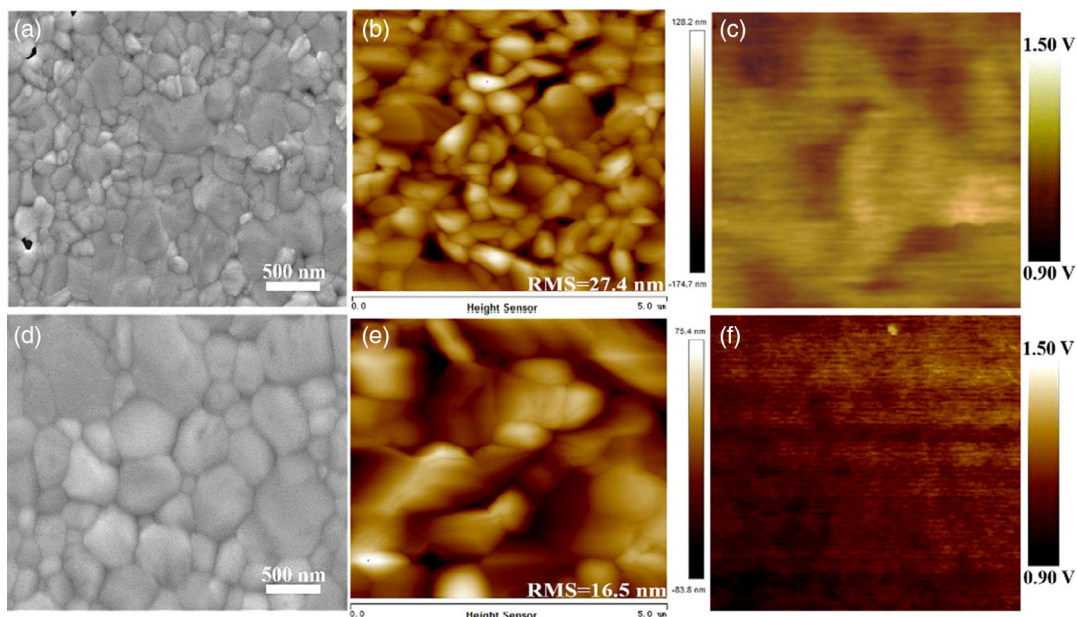


**Figure 1.** a,d) SEM, b,e) AFM, and c,f) KPFM images of HT-CsPbIBr<sub>2</sub> film (a–c) and VALT-CsPbIBr<sub>2</sub> film (d–f), respectively.

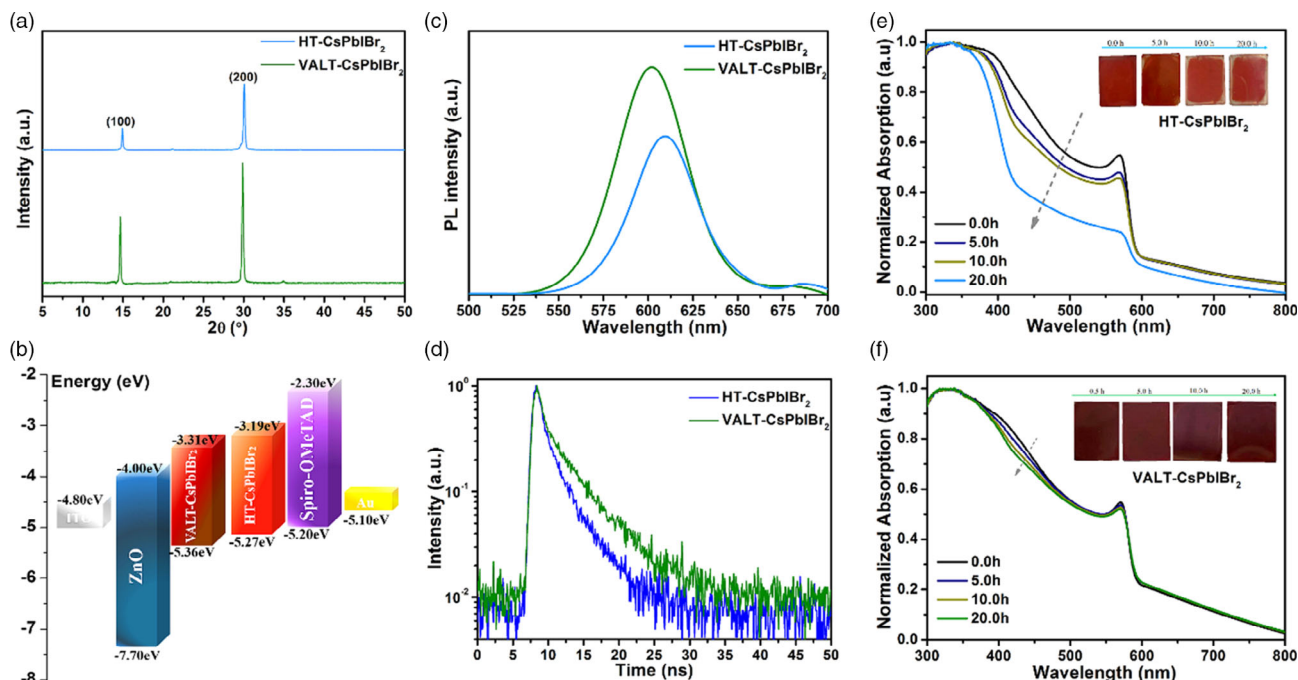


**Figure 2.** a) XRD patterns; b) energy level diagram of functional layers in PSCs of this work; c) steady PL spectra with quartz glasses as substrate; d) TRPL spectra with quartz glasses as substrate; e, f) time dependence of absorption spectra in the ambient environment ( $\approx 25^\circ\text{C}$ , 40–50% relative humidity), where two samples correspond to HT-CsPbIBr<sub>2</sub> and VALT-CsPbIBr<sub>2</sub>, respectively.

down-shifted VBM of VALT-CsPbIBr<sub>2</sub> could provide a larger built-in potential to achieve a higher  $V_{oc}$  for derived devices. Meanwhile, the deeper CBM of VALT-CsPbIBr<sub>2</sub> would reduce the electron transfer energy loss, which is beneficial for enhancing the efficiency of derived devices.<sup>[45–47]</sup> In addition, the Fermi level ( $E_F$ ) could be calculated according to  $E_F = 21.22 - E_{cutoff}$ , which corresponds to  $-4.04$  and  $-4.62$  eV for HT-CsPbIBr<sub>2</sub> and VALT-CsPbIBr<sub>2</sub> (Figure S7, Supporting Information), respectively. The deeper  $E_F$  of VALT-CsPbIBr<sub>2</sub> far away from its CBM not only agrees well with its larger work function but also confirms its weaker n-type doping feature once again.

As depicted in Figure 2c, VALT-CsPbIBr<sub>2</sub> shows a stronger photoluminescence (PL) peak coupled with a slight blueshift relative to HT-CsPbIBr<sub>2</sub>. Meanwhile, the PL peak located at the longer wavelength of VALT-CsPbIBr<sub>2</sub> is weaker than that of HT-CsPbIBr<sub>2</sub>, which is attributed to the weaker phase separation caused by fewer defects existing in the former.<sup>[48]</sup> In contrast, VALT-CsPbIBr<sub>2</sub> presents two different processes in the time-resolved photoluminescence (TRPL) measurement, which correspond to non-radiative recombination resulting from intrinsic defects ( $\tau_1 = 0.96$  ns) and radiative recombination ( $\tau_2 = 3.73$  ns, Figure 2d).<sup>[8]</sup> However, the non-radiative recombination process ( $\tau_1 = 4.77$  ns) is efficiently suppressed, yet the radiative recombination process ( $\tau_2 = 0.80$  ns) is highly promoted for VALT-CsPbIBr<sub>2</sub>, which coincides well with the higher crystallinity as well as fewer defects of VALT-CsPbIBr<sub>2</sub> relative to HT-CsPbIBr<sub>2</sub>.

Benefiting from the abovementioned physicochemical properties, VALT-CsPbIBr<sub>2</sub> not only exhibits stronger light-harvesting capability (Figure S8, Supporting Information) but also features

higher endurance to oxygen and moisture, which is intuitively confirmed by its almost unchanged film color and absorption spectra when placed in the ambient environment for 20 h (Figure 2e, f). Overall, the higher crystallinity, fewer intrinsic defects, deeper electronic energy level, and stronger light-harvesting capability of VALT-CsPbIBr<sub>2</sub> are favorable for obtaining superior efficiency and stability for derived devices.

To evaluate the photovoltaic performance of PSCs based on HT-CsPbIBr<sub>2</sub> film and VALT-CsPbIBr<sub>2</sub> film, the devices with the structure of ITO/ZnO/CsPbIBr<sub>2</sub>/Spiro/Au were fabricated (Figure 3a). The corresponding cross-sectional SEM image of VALT-CsPbIBr<sub>2</sub> PSCs is shown in Figure 3b, where all functional layers are uniformly stacked, and the thickness of VALT-CsPbIBr<sub>2</sub> film is  $\approx 315$  nm (Figure S9, Supporting Information). The current density–voltage ( $J$ – $V$ ) curves of optimized PSCs (measured under AM 1.5G irradiation at  $100\text{ mW cm}^{-2}$ ) are depicted in Figure 3c, and the corresponding photovoltaic parameters are summarized in Table 1.

As shown in Figure 3c, HT-CsPbIBr<sub>2</sub> PSCs produce a series of modest photovoltaic parameters, including  $V_{oc}$  of 1.235 V, short-circuit current density ( $J_{sc}$ ) of  $10.98\text{ mA cm}^{-2}$ , and FF of 66.34%, synthetically yielding a typical PCE of 9.00% with a large hysteresis index (HI) with a value of 18.89% (Figure S10 and Table S2, Supporting Information), where the HI is calculated according to the following equation.

$$HI = \frac{PCE_{RS} - PCE_{FS}}{PCE_{RS}} \quad (1)$$

where  $PCE_{RS}$  and  $PCE_{FS}$  represent the champion efficiency of derived devices measured via reverse and forward scans,

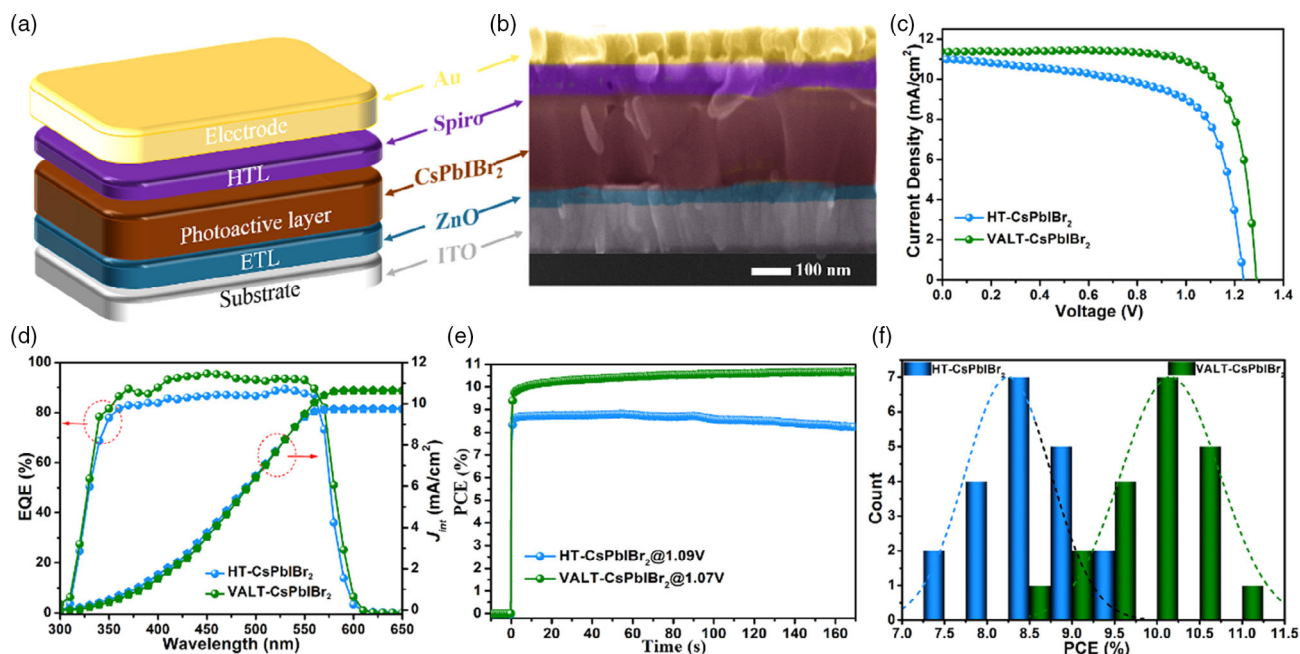


**Figure 3.** a) Schematic illustration and b) cross-sectional SEM image of VALT-CsPbIBr<sub>2</sub> PSCs; c) *J*–*V* curves measured from the reverse direction, d) EQE spectra coupled with *J*<sub>int</sub>, e) steady-state output of PCE at the maximum power point, and f) statistical histogram of PCE from 20 individual HT-CsPbIBr<sub>2</sub> PSCs and VALT-CsPbIBr<sub>2</sub> PSCs, respectively.

**Table 1.** Photovoltaic parameters of optimized devices.

Photoactive layer	<i>V</i> <sub>oc</sub> [V]	<i>J</i> <sub>sc</sub> [mA cm <sup>-2</sup> ]	FF [%]	PCE [%]	<i>J</i> <sub>int</sub> [mA cm <sup>-2</sup> ]	<i>α</i>	<i>KT/e</i>
HT-CsPbIBr <sub>2</sub>	1.235	10.98	66.34	9.00	9.92	0.969	1.98
VALT-CsPbIBr <sub>2</sub>	1.289	11.34	75.31	11.01	10.64	0.982	1.43

respectively.<sup>[20]</sup> Compared to HT-CsPbIBr<sub>2</sub> PSCs, VALT-CsPbIBr<sub>2</sub> PSCs display a distinct increase in all photovoltaic parameters with *V*<sub>oc</sub> of 1.289 V, *J*<sub>sc</sub> of 11.34 mA cm<sup>-2</sup>, and FF of 75.31%, then endowing an impressive PCE of 11.01% with reduced HI of 12.26%, where the superior efficiency is among the highest values of previously reported CsPbIBr<sub>2</sub> PSCs (Table S3, Supporting Information). The slightly higher *V*<sub>oc</sub> of VALT-CsPbIBr<sub>2</sub> PSCs should be ascribed to deeper VBM of VALT-CsPbIBr<sub>2</sub> film versus that of HT-CsPbIBr<sub>2</sub> film.<sup>[23]</sup> Meanwhile, the higher *J*<sub>sc</sub> and FF are not only due to the better morphology along with fewer defects of VALT-CsPbIBr<sub>2</sub> film but also closely correlate with the proficient charge dynamics of VALT-CsPbIBr<sub>2</sub> devices relative to HT-CsPbIBr<sub>2</sub> ones (discussed later).

In addition, VALT-CsPbIBr<sub>2</sub> PSCs display an intensified external quantum efficiency (EQE) value versus that of HT-CsPbIBr<sub>2</sub> PSCs in the range of 300–600 nm, especially the EQE value exceeding 90% from 400 to 560 nm, indicating better light-harvesting ability and efficient charge collection of the former. Moreover, the integrated current density (*J*<sub>int</sub>) of VALT-CsPbIBr<sub>2</sub> PSCs from the EQE spectrum is 10.64 mA cm<sup>-2</sup>, higher than that of HT-CsPbIBr<sub>2</sub> PSCs (9.92 mA cm<sup>-2</sup>), which is consistent with the trend of *J*<sub>sc</sub> in the *J*–*V* measurement. Note that the

discrepancy between *J*<sub>int</sub> and *J*<sub>sc</sub> should be attributed to the slow photovoltaic response and the spectral mismatch between the EQE source and solar simulator.<sup>[49,50]</sup>

As presented in Figure 3e, the steady-state PCE output is estimated to be ≈10.92% for VALT-CsPbIBr<sub>2</sub> devices after being measured for ≈170 s. In contrast, the HT-CsPbIBr<sub>2</sub> devices only present a lower PCE output of 8.60% accompanied by fluctuation, which correlates with their severe HI effect resulting from their more intrinsic defects.<sup>[40]</sup> The reproducibility of HT-CsPbIBr<sub>2</sub> PSCs and VALT-CsPbIBr<sub>2</sub> PSCs is evaluated in Figure 3f. As shown, the *J*–*V* histograms of 20 individual VALT-CsPbIBr<sub>2</sub> devices depict a narrow PCE distribution with an average value of 10.16%, while the corresponding value is only 8.25% for HT-CsPbIBr<sub>2</sub> PSCs, demonstrating the better repeatability of VALT-CsPbIBr<sub>2</sub> PSCs.

To shed light on the effect of charge dynamics on the photovoltaic performance of optimized devices, a series of characterizations were conducted. As depicted in Figure 4a, HT-CsPbIBr<sub>2</sub> PSCs present a slow photocurrent decay process with a large lifetime of 1.39 μs observed from the transient photocurrent (TPC) spectra. However, the photocurrent decay process of VALT-CsPbIBr<sub>2</sub> PSCs becomes much faster with a small lifetime of 0.76 μs, indicating VALT-CsPbIBr<sub>2</sub> PSCs featuring a more efficient charge extraction than HT-CsPbIBr<sub>2</sub> ones.<sup>[49,51]</sup> Meanwhile, the dependence of *J*<sub>sc</sub> on illumination intensity (*P*<sub>light</sub>) of VALT-CsPbIBr<sub>2</sub> PSCs presents a larger *α* (0.982) than that of HT-CsPbIBr<sub>2</sub> ones (*α* = 0.969, Figure 4b), where the larger *α* closer to unity revealing a perfecter charge extraction existing in the former.<sup>[47]</sup> The better charge extraction behavior of VALT-CsPbIBr<sub>2</sub> PSCs correlates with the smaller series resistance and larger recombination resistance determined from the

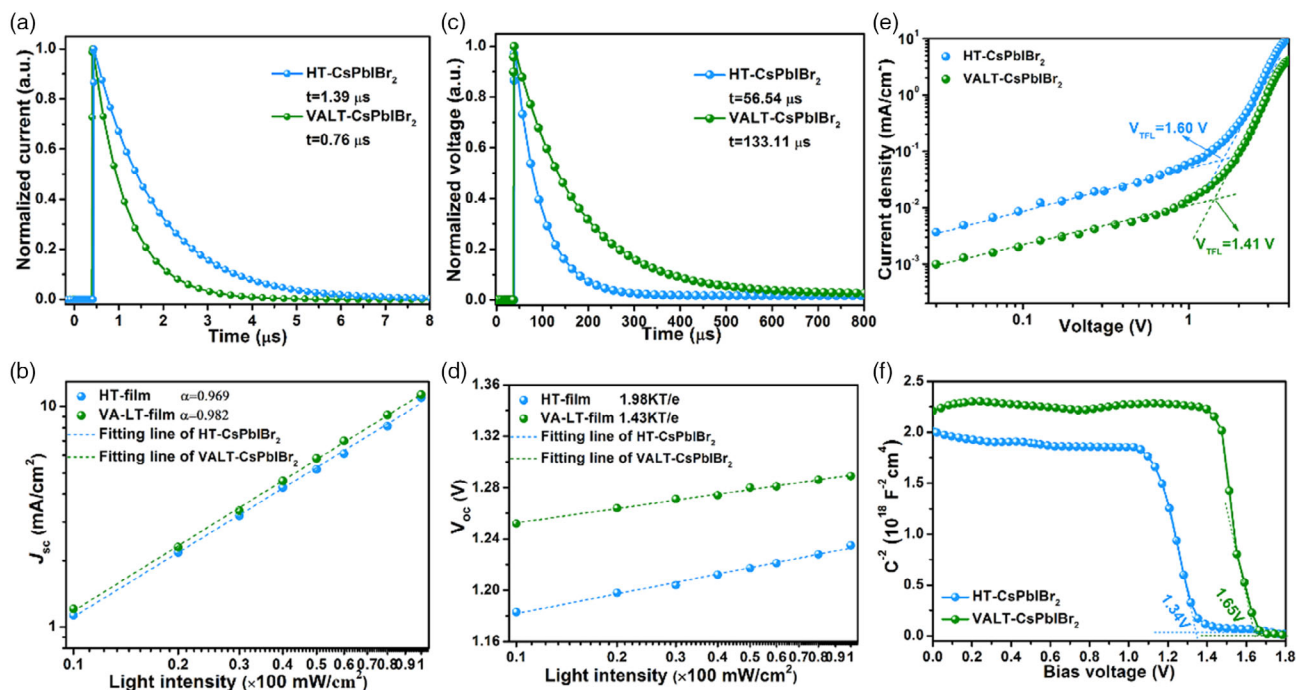


**Figure 4.** a) TPC, b)  $P_{\text{light}}$  depended on  $J_{\text{sc}}$ , c) TPV, d)  $P_{\text{light}}$  depended on  $V_{\text{oc}}$ , e) SCLC results of single-carrier devices with the structure of ITO/ZnO/CsPbIBr<sub>2</sub>/PCBM/Ag, and f) Mott–Schottky curves of PSCs based on HT-CsPbIBr<sub>2</sub> and VALT-CsPbIBr<sub>2</sub>, respectively.

electrochemical impedance spectra versus that of HT-CsPbIBr<sub>2</sub> (Figure S11, Supporting Information). Accordingly, the favorable charge extraction would be conducive to suppressing the bimolecular charge recombination and then improving the efficiency of derived devices.

To further gain insight into the charge recombination behavior in both optimized devices, the transient photovoltage (TPV) spectra and the  $P_{\text{light}}$  dependence of the  $V_{\text{oc}}$  of optimized devices were performed. As shown in Figure 4c, the HT-CsPbIBr<sub>2</sub> PSCs exhibit a fast photovoltage decay process with a small lifetime of 56.54  $\mu\text{s}$ . In contrast, VALT-CsPbIBr<sub>2</sub> PSCs show a slow photovoltage decay process with a prolonged lifetime of 133.11  $\mu\text{s}$ , implying the charge recombination rate is highly hindered for VALT-CsPbIBr<sub>2</sub> PSCs versus that of HT-CsPbIBr<sub>2</sub> ones.<sup>[19]</sup> Beyond that, a smaller ideality factor  $n$  of 1.43 also demonstrates that trap-assisted recombination is effectively suppressed in VALT-CsPbIBr<sub>2</sub> PSCs versus that of HT-CsPbIBr<sub>2</sub> ones (1.98).<sup>[52]</sup>

Furthermore, the trap-state densities ( $N_t$ ) of optimized devices were investigated via devices with the structure of ITO/ZnO/CsPbIBr<sub>2</sub>/PCBM/Ag according to the space charge-limited current (SCLC) method. In general, the  $J$ – $V$  curves of the abovementioned devices present three different regions, where the linear part in the lower voltage and the nonlinear section in the larger voltage correspond to the ohmic contact region and trap-filled region, respectively.<sup>[53]</sup> And the kink point between the abovementioned two regions is defined as the trap-filled limit voltage ( $V_{\text{TFL}}$ ), a factor to evaluate the  $N_t$ . And the  $N_t$  could be further calculated according to the following equation.

$$N_t = \frac{2V_{\text{TFL}}\epsilon_r\epsilon_0}{qL^2} \quad (2)$$

where the  $\epsilon_r$  and  $\epsilon_0$  denote the relative dielectric constant of CsPbIBr<sub>2</sub> (8) and the vacuum permittivity ( $\epsilon_0 = 8.85 \times 10^{-12} \text{ F m}^{-1}$ ), respectively;  $L$  represents the thickness of CsPbIBr<sub>2</sub> film (300 nm in this work) and  $q$  is the elementary charge ( $e = 1.60 \times 10^{-19} \text{ C}$ ).<sup>[49]</sup> Obviously, the VALT-CsPbIBr<sub>2</sub> PSCs show a relatively smaller  $V_{\text{TFL}}$  of 1.41 V than that of HT-CsPbIBr<sub>2</sub> PSCs ( $V_{\text{TFL}} = 1.60 \text{ V}$ ), demonstrating fewer  $N_t$  of  $1.38 \times 10^{16} \text{ cm}^{-3}$  of VALT-CsPbIBr<sub>2</sub> PSCs than that of HT-CsPbIBr<sub>2</sub> ones ( $N_t = 1.57 \times 10^{16} \text{ cm}^{-3}$ ), which should be ascribed to the relatively perfect crystals of the former.

In addition, the Mott–Schottky curves of optimized devices is depicted in Figure 4f, and the corresponding relationship is generally written with the equation

$$\frac{1}{C^2} = \frac{2}{q\epsilon_r\epsilon_0N_D} \left( V_{\text{bi}} - V - \frac{kT}{q} \right) \quad (3)$$

where  $C$  stands for the capacitance of the space charge region,  $V$  denotes the applied potential,  $V_{\text{bi}}$  is the built-in potential,  $k$  is the Boltzmann constant ( $1.38 \times 10^{-23} \text{ J K}^{-1}$ ),  $T$  refers to the absolute temperature (298.15 K, herein), and  $N_D$  corresponds to the doping density.<sup>[27]</sup> And then, the intercept of Mott–Schottky curves along the X-axis represents the  $V_{\text{bi}}$  of derived devices. As shown, HT-CsPbIBr<sub>2</sub> PSCs depict a small  $V_{\text{bi}}$  of 1.34 V, while the corresponding one shifts to 1.65 V for VALT-CsPbIBr<sub>2</sub> PSCs. In general, the larger  $V_{\text{bi}}$  of VALT-CsPbIBr<sub>2</sub> PSCs could provide a larger driving force for the photogenerated charge carrier separation and impart a wider depletion region to efficiently suppress charge recombination, being consistent well with the more proficient charge dynamics and superior photovoltaic performance of VALT-CsPbIBr<sub>2</sub> PSCs.<sup>[54,55]</sup>

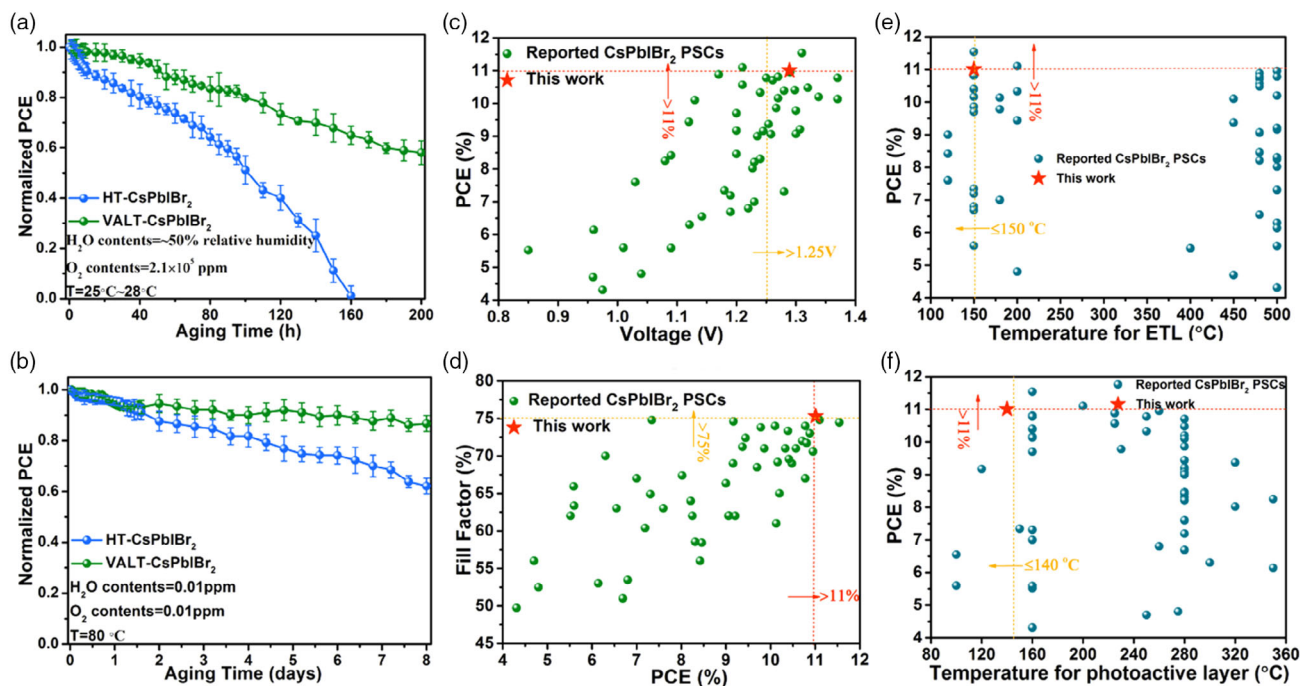


**Figure 5.** Time-dependent variations of normalized PCE of the unencapsulation HT-CsPbI<sub>2</sub>Br<sub>2</sub> PSCs and VALT-CsPbI<sub>2</sub>Br<sub>2</sub> PSCs a) storing in the ambient environment (25–28 °C, ≈50% relative humidity) and b) continuously heated at 80 °C in the glovebox (H<sub>2</sub>O < 1 ppm, O<sub>2</sub> < 1 ppm), respectively; photovoltaic parameters and fabrication parameters of CsPbI<sub>2</sub>Br<sub>2</sub> PSCs via different methods, where c) plots of PCE against V<sub>oc</sub>, d) plots of FF against PCE, e) plots of PCE against the temperature of ETL, and f) plots of PCE against the temperature of the photoactive layer.

Apart from the efficiency, both the long-term operational stability and fabrication technology of PSCs play a dominant role in the practical production of PSCs.<sup>[3]</sup> As exhibited in **Figure 5a**, the efficiency of HT-CsPbI<sub>2</sub>Br<sub>2</sub> PSCs presents fast degradation when placed in the ambient environment (25–28 °C, ≈50% relative humidity). Especially, the efficiency of HT-CsPbI<sub>2</sub>Br<sub>2</sub> PSCs is almost exhausted when placed in the ambient environment for 160 h. However, 65.0% of its initial value is retained for VALT-CsPbI<sub>2</sub>Br<sub>2</sub> PSCs when placed in the same atmosphere for 160 h. Moreover, 58.7% of its initial value is still unexpectedly preserved for VALT-CsPbI<sub>2</sub>Br<sub>2</sub> PSCs even with the storing time in the ambient environment extending for 200 h.

In addition, the efficiency of VALT-CsPbI<sub>2</sub>Br<sub>2</sub> PSCs shows a small decline with 87.1% of its initial value being kept after being continuously heated at 80 °C in a glovebox (H<sub>2</sub>O < 1 ppm, O<sub>2</sub> < 1 ppm) for nearly 8 days (Figure 5b). In contrast, the corresponding value only remained 61.7% for HT-CsPbI<sub>2</sub>Br<sub>2</sub> PSCs. Hence, VALT-CsPbI<sub>2</sub>Br<sub>2</sub> PSCs possess better long-term stability coupled with improved endurance against heat and moisture than HT-CsPbI<sub>2</sub>Br<sub>2</sub> PSCs.

Furthermore, VALT-CsPbI<sub>2</sub>Br<sub>2</sub> PSCs not only demonstrate impressive efficiency especially featuring a decent V<sub>oc</sub> of 1.289 V and a remarkable FF of 75.31% among the reported CsPbI<sub>2</sub>Br<sub>2</sub> PSCs (Figure 5c,d and Table S3, Supporting Information) but also present great potential in flexible PSCs due to their low-temperature processing procedure for either ETL or CsPbI<sub>2</sub>Br<sub>2</sub> photoactive layer (Figure 5e,f and Table S3, Supporting Information). Moreover, eliminating additional pretreatment (doping, precursor solution aging, etc.) or posttreatment

(interfacial passivation, applying optical modifying layer, etc.) but without sacrificing the photovoltaic performance of CsPbI<sub>2</sub>Br<sub>2</sub> PSCs via the VALT strategy should be promising for the low-cost industrial production of derived devices.

### 3. Conclusions

In summary, a simple dynamic vacuum-assisted low-temperature (merely 140 °C) processing technology was adopted for preparing high-quality CsPbI<sub>2</sub>Br<sub>2</sub> film. The as-prepared VALT-CsPbI<sub>2</sub>Br<sub>2</sub> film presents a smoother surface, more uniform full-coverage, and larger closely packed crystal grains coupled with fewer grain boundaries and defects relative to HT-CsPbI<sub>2</sub>Br<sub>2</sub> film processed via conventionally high temperature (280 °C). The stronger crystallinity with favorable characters impart intensified light-harvesting capability and extended charge carrier lifetime for VALT-CsPbI<sub>2</sub>Br<sub>2</sub> film. Consequently, VALT-CsPbI<sub>2</sub>Br<sub>2</sub> PSCs deliver an impressive PCE of 11.01% along with a remarkable FF of 75.31% versus that of HT-CsPbI<sub>2</sub>Br<sub>2</sub> ones (PCE = 9.00%, FF = 66.34%). The better photovoltaic performance of VALT-CsPbI<sub>2</sub>Br<sub>2</sub> PSCs correlates well with their lower trap-state densities, more proficient charge dynamics, and larger built-in potential than that of HT-CsPbI<sub>2</sub>Br<sub>2</sub> PSCs, which is intrinsically resulted from the superior physicochemical characteristics of the former. Moreover, VALT-CsPbI<sub>2</sub>Br<sub>2</sub> PSCs demonstrate better long-term stability accompanied by stronger endurance to moisture and heat than HT-CsPbI<sub>2</sub>Br<sub>2</sub> PSCs. Our work provides a facile method to fabricate efficient yet stable all-inorganic PSCs

via a low-temperature process, which would promote further research and industrial applications of the derived optoelectronic devices based on CsPbIBr<sub>2</sub>.

#### 4. Experiment Section

**Materials:** Cesium iodide (CsI, extra dry, 99.998%), lead bromide (PbBr<sub>2</sub>, extra dry, 99.99%), and DMSO (extra dry, 99.7%) were purchased from Sigma-Aldrich. 2,20,7,70-tetrakis (N,N-dip-methoxyphenylamine)-9,9-spirofluorene (Spiro-OMeTAD, 99.5%), bis(trifluoromethane) sulfonimide lithium salt (LiTFSI, 99%), 4-tert-butylpyridine (4-TBP, 96%), and [6,6]-phenyl-C61-butyric acid methyl ester (PCBM, 99%) were purchased from Xi'an Polymer Light Technology Corp. Indium tin oxide (ITO) conductive glass substrates (sheet resistance of 12–15 Ω sq<sup>-1</sup>) were purchased from Luminescence Technology Corporation. Unless otherwise noted, other chemicals were purchased from Energy Chemical Reagent Co., Ltd and used as received without further purification.

**Device Fabrication:** ITO substrates were successively cleaned via ultrasonic treatment in detergent, deionized water, ultrapure water, acetone, and isopropanol. Then, ITO substrates were dried with argon-flow and irradiated with oxygen plasma for 15 min. Following, the modified sol-gel-ZnO precursor solution was spin-coated upon ITO substrates at 3500 rpm for 25 s and then annealed at 150 °C for 40 min.<sup>[29]</sup> During the annealing process of ZnO film, 259.8 mg CsI and 367.0 mg PbBr<sub>2</sub> were dissolved in 1 mL DMSO and energetically stirred at room temperature until the mixture was completely dissolved. After the annealing process of ZnO, the ZnO film was irradiated with oxygen plasma for 5 min once again and then quickly moved into the glovebox. The CsPbIBr<sub>2</sub> precursor was spin-coated on ZnO film at 1000 rpm for 20 s and 3000 rpm for 30 s. The as-casted film was heated at 40 °C for 2 min and then was heated at 280 °C for 15 min for HT-CsPbIBr<sub>2</sub> film. In contrast, the as-casted film was quickly placed into a vacuum chamber to simultaneously vacuum and inflow argon (Ar) to maintain the pressure at 50–100 Pa and keep the annealing temperature located at 140 °C after annealing 40 °C for 2 min for preparing VALT-CsPbIBr<sub>2</sub> film. Subsequently, Spiro-OMeTAD (72.3 mg), Li-TFSI (17.5 μL, 520 mg mL<sup>-1</sup> in acetonitrile), and 4-TBP (28.8 μL) were added to 1 mL of chlorobenzene, stirred for at least 0.5 h under darkness, filtered with a 0.22 μm filter, and then spin-coated upon CsPbIBr<sub>2</sub> film (4000 rpm, 30 s). Following, the as-prepared film was placed into a homemade container (Figure S12, Supporting Information) with high purity oxygen atmosphere for at least 5.0 h. (Note that the devices with Spiro-OMeTAD being oxidated under different atmospheres for different times are performed in Figure S13, Supporting Information.) Finally, the sample was placed into a vacuum chamber and Au (≈100 nm) was deposited at a vacuum of ≈2 × 10<sup>-4</sup> Pa. A shadow mask with 0.04 cm<sup>2</sup> was used to define the photoactive area of the final devices.

**Device Characterization:** The J–V characteristics of PSCs were measured via Keithley 2400 source-meter under AM 1.5G illumination via a Newport-Oriel solar simulator, where the light intensity was calibrated to 100 mW cm<sup>-2</sup> using an NREL-certified single-crystal silicon cell. The EQE spectra were measured with a commercial photomodulation spectroscopic setup that included a Xenon lamp, an optical chopper, a monochromator, and a lock-in amplifier operated via a PC computer. Meanwhile, a calibrated Si photodiode was used as a standard in the EQE measurement.

#### Supporting Information

Supporting Information is available from the Wiley Online Library or from the author.

#### Acknowledgements

J.H. and S.H. contributed equally to this work. This work was financially supported by the Science and Technology Development Project of Henan

Province (No. 202300410057), the Postdoctoral Fund of China (No. FJ3050A0670111), and the National Natural Science Foundation of China (No. 21776144, No. 61704047).

#### Conflict of Interest

The authors declare no conflict of interest.

#### Data Availability Statement

The data that support the findings of this study are available from the corresponding author upon reasonable request.

#### Keywords

CsPbIBr<sub>2</sub>, inorganic perovskites, low-temperature engineering, solar cells, stability

Received: October 11, 2021

Revised: December 6, 2021

Published online:

- [1] J. Tian, Q. Xue, Q. Yao, N. Li, C. J. Brabec, H. L. Yip, *Adv. Energy Mater.* **2020**, *10*, 2000183.
- [2] H. Zhu, Y. Ren, L. Pan, O. Ouellette, F. T. Eickemeyer, Y. Wu, X. Li, S. Wang, H. Liu, X. Dong, S. M. Zakeeruddin, Y. Liu, A. Hagfeldt, M. Gratzel, *J. Am. Chem. Soc.* **2021**, *143*, 3231.
- [3] N.-G. Park, K. Zhu, *Nat. Rev. Mater.* **2020**, *5*, 333.
- [4] NREL, <https://www.nrel.gov/pv/assets/pdfs/best-research-cell-efficiencies-rev211117.pdf>, **2020** (accessed: November 2021).
- [5] R. Cheacharoen, N. Rolston, D. Harwood, K. A. Bush, R. H. Dauskardt, M. D. McGehee, *Energ. Environ. Sci.* **2018**, *11*, 144.
- [6] G. Zheng, C. Zhu, J. Ma, X. Zhang, G. Tang, R. Li, Y. Chen, L. Li, J. Hu, J. Hong, Q. Chen, X. Gao, H. Zhou, *Nat. Commun.* **2018**, *9*, 2793.
- [7] H. Zheng, G. Liu, X. Xu, S. Xu, X. Zhang, C. Zhang, T. Hayat, X. Pan, *Sol. RRL* **2019**, *3*, 1800276.
- [8] Y. Guo, X. Yin, J. Liu, W. Que, *J. Mater. Chem. A* **2019**, *7*, 19008.
- [9] F. Yang, D. Hirotsu, G. Kapil, M. A. Kamarudin, C. H. Ng, Y. Zhang, Q. Shen, S. Hayase, *Angew. Chem., Int. Ed.* **2018**, *57*, 12745.
- [10] Q. Tai, K.-C. Tang, F. Yan, *Energ. Environ. Sci.* **2019**, *12*, 2375.
- [11] S. Dastidar, C. J. Hawley, A. D. Dillon, A. D. Gutierrez-Perez, J. E. Spanier, A. T. Fafarman, *J. Phys. Chem. Lett.* **2017**, *8*, 1278.
- [12] Z. Liu, B. Sun, X. Liu, J. Han, H. Ye, T. Shi, Z. Tang, G. Liao, *Nano-Micro Lett.* **2018**, *10*, 34.
- [13] W. Chen, H. Chen, G. Xu, R. Xue, S. Wang, Y. Li, Y. Li, *Joule* **2019**, *3*, 191.
- [14] M. Yue, J. Su, P. Zhao, Z. Lin, J. Zhang, J. Chang, Y. Hao, *Nano-Micro Lett.* **2019**, *11*, 91.
- [15] W. Li, M. U. Rothmann, A. Liu, Z. Wang, Y. Zhang, A. R. Pascoe, J. Lu, L. Jiang, Y. Chen, F. Huang, Y. Peng, Q. Bao, J. Etheridge, U. Bach, Y. B. Cheng, *Adv. Energy Mater.* **2017**, *7*, 1700946.
- [16] J. Wang, P. Zhao, Y. Hu, Z. Lin, J. Su, J. Zhang, J. Chang, Y. Hao, *Sol. RRL* **2021**, *5*, 2100121.
- [17] F. H. Alharbi, S. Kais, *Renew. Sust. Energ. Rev.* **2015**, *43*, 1073.
- [18] H. Zhao, Y. Han, Z. Xu, C. Duan, S. Yang, S. Yuan, Z. Yang, Z. Liu, S. Liu, *Adv. Energy Mater.* **2019**, *9*, 1902279.
- [19] W. Zhu, Q. Zhang, D. Chen, Z. Zhang, Z. Lin, J. Chang, J. Zhang, C. Zhang, Y. Hao, *Adv. Energy Mater.* **2018**, *8*, 1802080.
- [20] Y. Wang, K. Wang, W. S. Subhani, C. Zhang, X. Jiang, S. Wang, H. Bao, L. Liu, L. Wan, S. F. Liu, *Small* **2020**, *16*, e1907283.



- [21] J. Du, J. Duan, X. Yang, Y. Duan, Q. Zhou, Q. Tang, *Angew. Chem., Int. Ed.* **2021**, *60*, 10608.
- [22] W. S. Subhani, K. Wang, M. Du, X. Wang, S. Liu, *Adv. Energy Mater.* **2019**, *9*, 1803785.
- [23] W. Zhu, Z. Zhang, W. Chai, Q. Zhang, D. Chen, Z. Lin, J. Chang, J. Zhang, C. Zhang, Y. Hao, *ChemSusChem* **2019**, *12*, 2318.
- [24] Y. You, W. Tian, M. Wang, F. Cao, H. Sun, L. Li, *Adv. Mater. Interfaces* **2020**, *7*, 2000537.
- [25] C. Zhang, K. Wang, Y. Wang, W. S. Subhani, X. Jiang, S. Wang, H. Bao, L. Liu, L. Wan, S. Liu, *Sol. RRL* **2020**, *4*, 2000254.
- [26] W. Zhu, Z. Zhang, D. Chen, W. Chai, D. Chen, J. Zhang, C. Zhang, Y. Hao, *Nano-Micro Lett.* **2020**, *12*, 87.
- [27] X. Jiang, W. S. Subhani, K. Wang, H. Wang, L. Duan, M. Du, S. Pang, S. Liu, *Adv. Mater. Interfaces* **2021**, *8*, 2001994.
- [28] D. Wang, W. Li, R. Li, W. Sun, J. Wu, Z. Lan, *Sol. RRL* **2021**, 2100375.
- [29] H. Wang, S. Cao, B. Yang, H. Li, M. Wang, X. Hu, K. Sun, Z. Zang, *Sol. RRL* **2019**, *4*, 1900363.
- [30] X. Li, D. Bi, C. Yi, J.-D. Décoppet, J. Luo, S. M. Zakeeruddin, A. Hagfeldt, M. Grätzel, *Science* **2016**, *353*, 58.
- [31] C. Chen, L. Zeng, Z. Jiang, Z. Xu, Y. Chen, Z. Wang, S. Chen, B. Xu, Y. Mai, F. Guo, *Adv. Funct. Mater.* **2021**, 2107644.
- [32] S. R. Pathipati, *J. Lumin.* **2021**, *239*, 118345.
- [33] C. Liu, W. Li, J. Chen, J. Fan, Y. Mai, R. E. I. Schropp, *Nano Energy* **2017**, *41*, 75.
- [34] N. Li, Z. Zhu, J. Li, A. K. Y. Jen, L. Wang, *Adv. Energy Mater.* **2018**, *8*, 1800525.
- [35] J. Lu, S.-C. Chen, Q. Zheng, *ACS Appl. Energ. Mater.* **2018**, *1*, 5872.
- [36] M. J. Carnie, C. Charbonneau, M. L. Davies, J. Troughton, T. M. Watson, K. Wojciechowski, H. Snaith, D. A. Worsley, *Chem. Commun.* **2013**, *49*, 7893.
- [37] S. Han, H. Zhang, R. Wang, Q. He, *Mater. Sci. Semicon. Proc.* **2021**, *131*, 105847.
- [38] Y. Gao, Z. Shen, F. Tan, G. Yue, R. Liu, Z. Wang, S. Qu, Z. Wang, W. Zhang, *Nano Energy* **2020**, *76*, 104964.
- [39] W. Chai, J. Ma, W. Zhu, D. Chen, H. Xi, J. Zhang, C. Zhang, Y. Hao, *ACS Appl. Mater. Inter.* **2021**, *13*, 2868.
- [40] Z. Zhang, D. Chen, W. Zhu, J. Ma, W. Chai, D. Chen, J. Zhang, C. Zhang, Y. Hao, *Sci. China Mater.* **2021**, *64*, 2107.
- [41] Z. Zhang, F. He, W. Zhu, D. Chen, W. Chai, D. Chen, H. Xi, J. Zhang, C. Zhang, Y. Hao, *Sustain. Energy Fuels* **2020**, *4*, 4506.
- [42] C. F. J. Lau, X. Deng, Q. Ma, J. Zheng, J. S. Yun, M. A. Green, S. Huang, A. W. Y. Ho-Baillie, *ACS Energy Lett.* **2016**, *1*, 573.
- [43] M. Aamir, T. Adhikari, M. Sher, N. Revaprasadu, W. Khalid, J. Akhtar, J.-M. Nunzi, *New J. Chem.* **2018**, *42*, 14104.
- [44] J. Liang, Z. Liu, L. Qiu, Z. Hawash, L. Meng, Z. Wu, Y. Jiang, L. K. Ono, Y. Qi, *Adv. Energy Mater.* **2018**, *8*, 1800504.
- [45] Y. Gao, Z. Wang, G. Yue, X. Yu, X. Liu, G. Yang, F. Tan, Z. Wei, W. Zhang, *Sol. RRL* **2019**, *3*, 1900012.
- [46] X. Gao, Z. Su, S. Qu, W. Zhang, Y. Gao, S. He, Z. Wang, S. Lu, G. Dong, G. Yue, F. Tan, Z. Wang, *J. Mater. Chem. C* **2021**, *9*, 13500.
- [47] D. Chen, B. Tian, G. Fan, Y. Wang, W. Zhu, Z. Ren, H. Xi, K. Su, J. Zhang, C. Zhang, J. Zhang, Y. Hao, *ACS Appl. Energy Mater.* **2021**, *4*, 5661.
- [48] Q. Ma, S. Huang, X. Wen, M. A. Green, A. W. Y. Ho-Baillie, *Adv. Energy Mater.* **2016**, *6*, 1502202.
- [49] D. Wang, W. Li, X. Liu, G. Li, L. Zhang, R. Li, W. Sun, J. Wu, Z. Lan, *ACS Appl. Energy Mater.* **2021**, *4*, 5747.
- [50] W. Li, B. Zhu, M. U. Rothmann, A. Liu, W. Chen, Y. Y. Choo, N. Pai, W. Mao, T. Zhang, Q. Bao, X. Wen, U. Bach, J. Etheridge, Y.-B. Cheng, *Sci. China Mater.* **2021**, *64*, 2655.
- [51] Y. Gao, M. Cui, S. Qu, H. Zhao, Z. Shen, F. Tan, Y. Dong, C. Qin, Z. Wang, W. Zhang, Z. Wang, Y. Lei, *Small* **2021**, 2104623 <https://doi.org/10.1002/smll.202104623>.
- [52] L. Gong, J.-S. Zhang, C. Wang, H. Fu, Y.-F. Lu, J.-L. Chen, J.-C. Fan, Z.-S. Chao, *ACS Appl. Energ. Mater.* **2021**, *4*, 4686.
- [53] S. Cao, H. Wang, H. Li, J. Chen, Z. Zang, *Chem. Eng. J.* **2020**, *394*, 124903.
- [54] Q. Dong, C. Zhu, M. Chen, C. Jiang, J. Guo, Y. Feng, Z. Dai, S. K. Yadavalli, M. Hu, X. Cao, Y. Li, Y. Huang, Z. Liu, Y. Shi, L. Wang, N. P. Padture, Y. Zhou, *Nat. Commun.* **2021**, *12*, 973.
- [55] Z. Liu, L. Qiu, L. K. Ono, S. He, Z. Hu, M. Jiang, G. Tong, Z. Wu, Y. Jiang, D.-Y. Son, Y. Dang, S. Kazaoui, Y. Qi, *Nat. Energy* **2020**, *5*, 596.